JOURNAL OF SOLID STATE CHEMISTRY 41, 75–89 (1982)

On the Structures of the Intermediate Phases in the Terbium Oxide System

R. T. TUENGE AND L. EYRING

Department of Chemistry, and the Center for Solid State Science, Arizona State University, Tempe, Arizona 85287

Received July 13, 1981; in final form September 18, 1981

A high-resolution transmission electron microscope investigation of the ordered phases in the terbium oxide system in the range $1.714 < O/Tb < 2$ has been performed. Two ordered phases belonging to the R_nO_{2n-2} homologous series of defective fluorite phases have been examined, namely, the $n = 11$ and $n = 12$ members. Selected area electron diffraction has revealed two polymorphs of the $n = 12$ phase in the TbO_x system. In addition, a metastable $n = 16$ phase was identified by diffraction and imaging techniques. High-resolution (~3 Å) images of thin crystals of these phases are presented. Computer-simulated lattice images based on dynamical scattering theory with the incorporation of the appropriate instrumental parameters at through-focus and through-thicknesses for proposed defect structures of the intermediate terbium oxide phases are presented for comparison. Images calculated at optimum defocus and periodic thicknesses correspond to the projected crystal potential. The remarkably good match between experimental and calculated images at optimum defocus and in a through-focus series supports the choice of the structural models for the real defect structure of the intermediate phases.

Introduction

The value of high-resolution transmission electron microscopy (HRTEM) as a complementary technique for crystal structure determination has been clearly demonstrated in recent years (*1*). A considerable number of intergrowth structures and stacking sequences of polytype compounds have been determined by lattice imaging techniques. In a few studies actual atom positions have been obtained by structure imaging under conditions where there is a one-to-one correspondence between image contrast and rows of atoms. Using this method with the employment of multiple-beam dynamical scattering calculations, Skarnulis *et al.* (*2*) have refined the structure of "$GeNb_9O_{25}$." In an extension of this technique to close-packed structures, a detailed comparison of experimental and calculated structure images have resulted in proposed crystal structures for several praseodymium oxides (*3*, *4*).

Rare earth oxides are becoming increasingly important in industry because of the wide variety of physical, chemical, and electronic properties which they display. In the electronics industry as an example, they are used as insulators in high-electric-field devices and as improved-efficiency phosphors.

For most rare earths the highest oxide known is the sesquioxide. However, cerium, praseodymium, and terbium, which have relatively stable tetravalent oxidation states, form oxides in the composition range RO_x ($1.5 \leq x \leq 2.0$). These three

0022-4596/82/010075-15$02.00/0

oxide systems are known to exhibit ordered phases which comprise a homologous series with formula R_nO_{2n-2} (n an integer between 4 and ∞) (*5*). Four intermediate phases, corresponding to $n = 7$, 9, 10, and 11 were identified in the CeO_{2-x} system by Ray *et al.* (*6*) in an X-ray and neutron diffraction study. Recently, the defect structure of the ordered intermediate phases in the praseodymium oxide system Pr_9O_{16} (ζ phase, $n = 9$), $Pr_{40}O_{72}$ (ϵ phase, $n = 10$), $Pr_{88}O_{160}$ (δ (2) phase, $n = 11$), and $Pr_{24}O_{44}$ (β phase, $n = 12$) has been investigated by electron diffraction and high-resolution crystal structure imaging (*3*, *4*). The present work extends the structural study of the R_nO_{2n-2} series of phases to the terbium oxide system.

A phase diagram of the TbO_x system is shown in Fig. 1. It is constructed from both isobaric and isothermal tensimetric studies (*7*, *8*), and the electron diffraction work of Kunzmann and Eyring (*9*) on hydrothermally grown crystals. Tb_2O_3 exists in two of the three polymorphs known for the rare earth sesquioxides: the body-centered cubic C-form and the monoclinic B-form. The structural relationship between the cubic sesquioxide and the fluorite dioxide has been described (*5*) as a removal of one-fourth of the oxygen atoms along noninter-

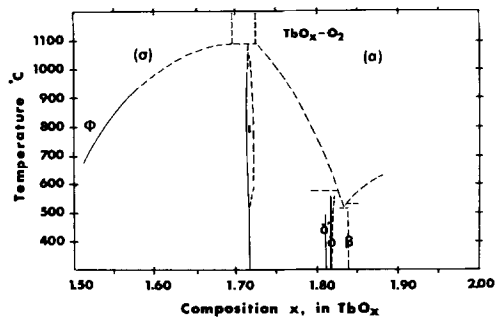

FIG. 1. The phase diagram of the TbO_x system. The dashed curves mark the boundaries of the disordered α and σ regions suggested by electron microscopic studies.

secting strings of four ⟨111⟩ directions such that every metal is six-coordinate. The monoclinic B-type has been viewed by Caro (*10*) as a slight distortion from the hexagonal A-form in the stacking of $(RO)_n^{n+}$ layers.

Early X-ray powder diffraction studies (*11*) have determined a rhombohedral cell for Tb_7O_{12}, ι phase, and have shown that the structure is isomorphous to that of the same member in the Ce and Pr oxide systems. The structure of this phase is well established (*12*, *13*) and consists of strings of oxygen vacancies in the ⟨111⟩ direction of the rhombohedral unit cell.

For the intermediate phase $Tb_{11}O_{20}$, δ phase, Kunzmann and Eyring (*9*) have established a triclinic cell with parameters: $a = 6.5$ Å, $b = 9.9$ Å, $c = 6.5$ Å, $\alpha = 90.0°$, $\beta = 99.6°$, and $\gamma = 96.3°$. The **a** and **c** axes in this structure are both $\frac{1}{2}[211]$ fluorite vectors, a feature common to the odd members of the homologous series in the Pr and Tb oxide systems.

A monoclinic cell was also observed in the electron diffraction studies (*9*) for the $n = 12$ member, β phase, of the series in the TbO_x system. The cell volume for this member is twice that established for the β phase in the PrO_x system ($Pr_{24}O_{44}$) due to a doubling of the **b** axis.

As part of the work described in this paper, electron diffraction and imaging techniques are used to investigate the phase formation in the Tb_nO_{2n-2} homologous series. A new $n = 12$, β phase, polymorph is described here and a metastable phase for $n = 16$ is reported. The major portion of this paper is concerned with the elucidation of the crystal structures of δ phase and the two β-phase polymorphs in the Tb_nO_{2n-2} system. Attempts to determine the structures using X-ray diffraction from either powders or single crystals of these intermediate phases have been unsuccessful due to the combined effects of the relatively small X-ray scattering factor for oxygen, the high

X-ray absorption by terbium and the extensive microtwinning and faults in prepared crystals. On the other hand, the success of crystal structure imaging for structure determination of the fluorite-related praseodymium oxides suggested that this technique should be applied to the intermediate phases in the TbO_x system.

Experimental Procedure

Crystals of terbium oxide with composition TbO_x ($1.714 < x < 2$) were prepared from 5:1 weight ratio of HNO_3 and 99.999% terbium oxide powder (Research Chemicals) by a hydrothermal growth technique (*14*). The high nitric acid ratio was used in order to increase the oxygen content of the crystals. The steps in the growth procedure were: (1) hydrothermal pressure raised to 23,900 psi, (2) isobaric temperature increase to 820°C, (3) oscillatory stepwise depressurization to 15,800 psi over 30 hr, (4) isobaric cooling to 400°C, (5) depressurization to 10,000 psi, (6) cool and depressurize to ambient. The crystals were soaked in 0.2*N* HNO_3 for 3 days to dissolve any hydroxide coating.

The 0.1- to 0.5-mm-sized crystals obtained from the high-pressure treatment were predominantly black in color with small amounts of red material adhering to them. Guinier powder diffraction patterns indicated that the major phase constituting the black material was $Tb_{11}O_{20}$.

The technique of specimen preparation for high-resolution electron microscope imaging and the procedure for microscope observation was that described by Iijima (*15*). The oxide crystals which were

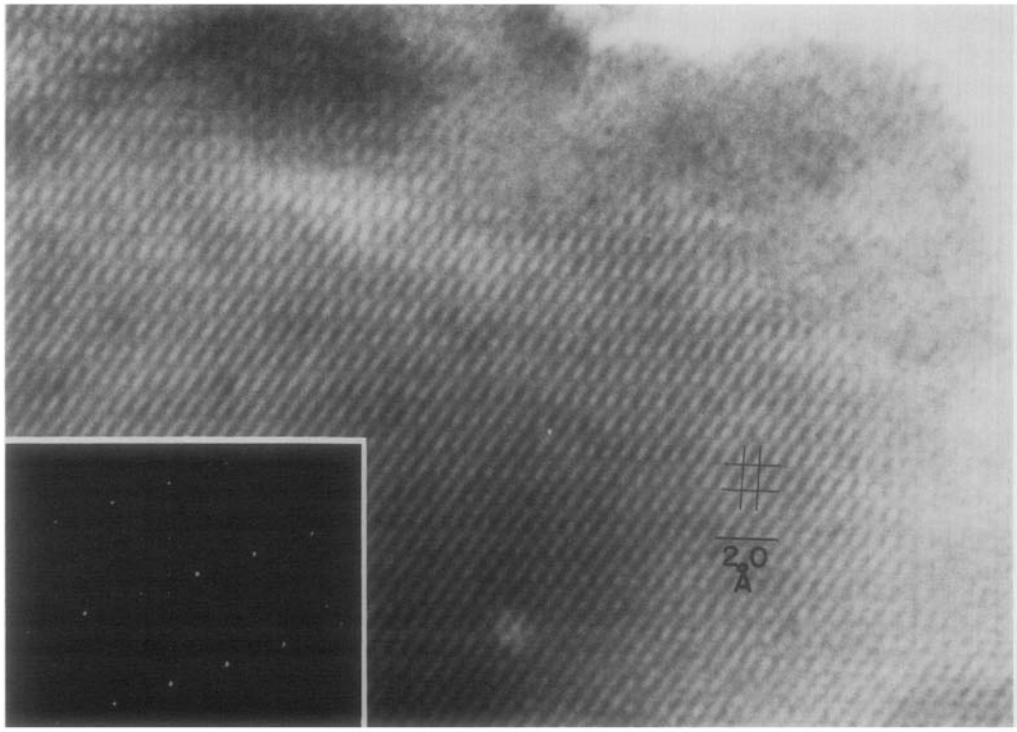

FIG. 2. An observed image of the δ phase, $Tb_{11}O_{20}$, taken with the electron beam parallel to the $\langle 100 \rangle_{11}$ axis.

crushed under liquid nitrogen were suspended on a holey carbon supporting film. Observations were made with a modified JEM 100B electron microscope with a 30° tilting stage. Image photographs were usually taken at 900-Å underfocus with a direct magnification of about 5×10^5.

Results and Discussion

δ Phase—$Tb_{11}O_{22}$

A bright-field HRTEM image with an inset electron diffraction pattern of a crystal of $Tb_{11}O_{20}$ is shown in Fig. 2. The crystal fragment was oriented so that the incident electron beam was parallel to the **a** axis of the triclinic cell. The image was obtained using a 40-μm objective aperture at a defocus value of about −900 Å from a thin area near the edge of the crystallite where the thickness should be less than 60 Å (inside the first equal-thickness contour). The conditions of the specimen and microscope were favorable, according to the technique developed by Cowley and Iijima (*16*), for the image to be a linear representation of the crystal structure.

For close-packed structures such as the fluorite related oxides, ordered vacant lattice sites that cause the neighboring atoms to recede produce the largest variation in the crystal potential, although not as large as that resulting from more open structures. At sufficiently high resolution then, the projection of rows of oxygen vacancies should appear as bright contrast in the image. The micrograph in Fig. 2 does, indeed, reveal two bright spots per two-dimensional repeat unit. However, to provide a complete and accurate interpretation of the experimental image contrast in terms of atom positions, it is necessary to include calculations based on the dynamical scattering of electrons in the crystal. For this study the *n*-beam multislice method (*17, 18*) was used to calculate the object wavefield with effects due to defocusing, spherical aberration, incoherence, and size of the objective aperture inserted to produce the image intensity distribution. The computations were performed with the aid of Fortran

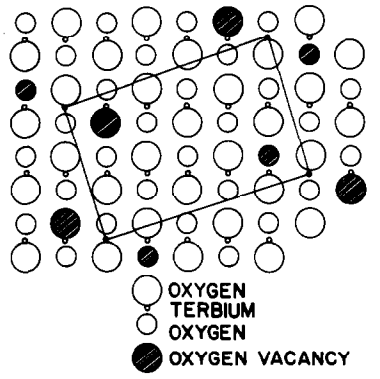

FIG. 3. The projection of the delta structure along the $\langle 100\rangle_{11} = \langle 21\bar{1}\rangle_F$. Small dark circles represent metal atoms, larger circles mark rows of oxygen atoms.

TABLE I

ATOM POSITIONS[a] FOR THE PROPOSED STRUCTURE OF δ PHASE, $Tb_{11}O_{20}$, SYMMETRY $P\bar{1}$

	x	*y*	*z*
Atom			
Tb1	0.000	0.000	0.000
Tb2	0.288	0.089	0.576
Tb3	0.575	0.191	0.086
Tb4	0.058	0.383	0.191
Tb5	0.818	0.273	0.636
Tb6	0.364	0.455	0.727
Oxygen vacancy			
O2	0.955	0.068	0.659
O3	0.046	0.432	0.841
O4	0.409	0.886	0.568
O5	0.318	0.023	0.886
O6	0.682	0.477	0.614
O7	0.500	0.250	0.750
O8	0.136	0.795	0.023
O9	0.864	0.705	0.477
O10	0.409	0.386	0.068
O11	0.227	0.659	0.705

[a] Anion positions are all ideal fluorite positions. Cation positions are relaxed from ideal fluorite positions by a transformation from the refined ι-phase (Tb_7O_{12}) cation positions.

computer programs developed by Skarnulis *et al.* (*19*) and O'Keefe (*20*).

An **a**-axis projection of the $Tb_{11}O_{20}$ structure proposed by Kunzmann and Eyring (*9*) is shown in Fig. 3. The vacancy arrangement (shaded circles) was based on the fact that the **a**–**c** plane is common to all odd members of the R_nO_{2n-2} series of phases in the Pr and Tb oxide systems suggesting that oxygen vacancies occur in pairs and form a two-dimensionally periodic structure identical to that found in the refined structure of the $n = 7$ phase. The separation between layers with vacancy doublets is n rows of metal atoms in the **b**-axis direction. Recent HRTEM images with accompanying calculated images (*3*) indicate that this model is valid for the $n = 9$ member in the PrO_x system.

A series of calculated crystal structure images of $Tb_{11}O_{20}$ based on the atom positions listed in Table I with variation due to crystal thickness and defocus is displayed in Fig. 4. The multislice calculation used the 6.5-Å **a**-axis length for the slice thickness. Amplitudes were obtained for a total of 569 diffracted beams, 19 of which passed through the 0.285-$Å^{-1}$ radius of the objective aperture. It is apparent that a one-to-one correspondence of white spots to the projected vacancy positions results only for a crystal thickness of 26 Å at a defocus of −900 Å. Further calculations have shown that this "linear image" extends up to the first extinction distance of about 60 Å for the $Tb_{11}O_{20}$.

The experimental thin-crystal image of $Tb_{11}O_{20}$ (Fig. 2) reproduces the contrast of the pattern calculated at 26-Å thickness and −900 Å defocus very well. This demonstrates that in this case the vacancies in the terbium oxide superstructure are imaged directly. The brighter area in the lower right in Fig. 2 could be due to additional oxygen vacancies (clusters) in several of the cells along this projection since the crystal is only 4–6 unit cells thick here.

Since regions of crystalline fragments as thin as that seen in Fig. 2 are not often imaged from specimens prepared by the

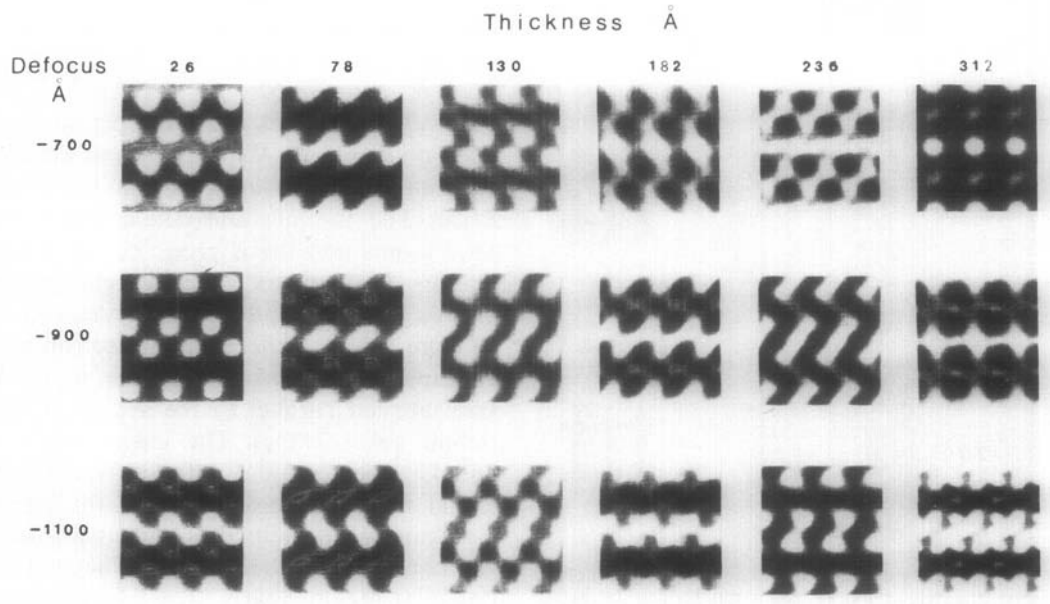

FIG. 4. Calculated $\langle 100 \rangle_{11}$ crystal structure images of the proposed model of the δ phase, $Tb_{11}O_{20}$.

fracture technique, any structural information obtained from thicker areas would be valuable. Images similar to the crystal structure image are calculated for a 130-Å thickness at −700 Å and a 236-Å thickness at −1100 Å defocus. They both display two bright spots per cell but are distorted from the projected vacancy positions. Extreme care must be exercised in interpretation of thicker crystal images that do not reflect the projected crystal potential. The projection of the unit cell, however, can always be recognized.

It can be seen in Fig. 4 that the image is very sensitive to the focusing conditions. Figure 5 shows a comparison of calculated and experimental images of $Tb_{11}O_{20}$ at 100 Å thickness and defocus values of −900, −1100, and −1200 Å. Although the intensity distributions differ greatly with defocus, the similarity between calculated and experimental images is evident.

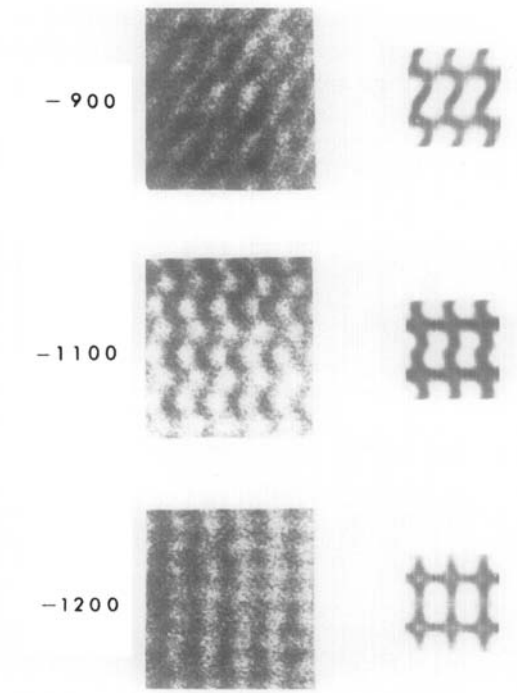

FIG. 5. Comparison of calculated and experimental $\langle 100\rangle_{11}$ images of $Tb_{11}O_{20}$ for a 100-Å-thick crystal at different defocus conditions.

β-Phase Polymorphs

Electron diffraction patterns of the two $n = 12$ polymorphs found in the terbium oxide system are shown in Fig. 6. Both selected area patterns were obtained with the crystal oriented such that the electron beam was aligned with the $[21\bar{1}]$ direction of the fluorite subcell. The pattern in Fig. 6a, which had not previously been observed, displays 24 weak superstructure reflections along the fluorite $\langle\bar{6}8\bar{4}\rangle$ direction and 6 along the $\langle 022\rangle_F$ direction. Choosing the **a** axis of the superstructure along $\langle 211\rangle_F$, a common feature of all members of the R_nO_{2n-2} homologous series of fluorite-related phases, a triclinic cell can be defined having the axial relationships:

$$a = a_F + \tfrac{1}{2}b_F + \tfrac{1}{2}c_F,$$

$$b = a_F + \tfrac{3}{2}b_F + \tfrac{3}{2}c_F,$$

$$c = a_F - \tfrac{3}{2}b_F + \tfrac{3}{2}c_F,$$

where the subscripts refer to the fluorite parameters. The lattice parameters for this β-phase polymorph, which will be designated β(2), are $a = 6.4$ Å, $b = 12.24$ Å, $c = 12.24$ Å, $\alpha = 79.52°$, $\beta = 100.03°$, $\gamma = 69.63°$. These values are ideal parameters based on $a = 5.22$ Å for TbO_2 and do not take into account distortions from the basic lattice. The triclinic unit cell contains 24 metal atoms and the β phase composition requires 4 vacant oxygen sites giving the formula $Tb_{24}O_{44}$ for this new polymorph.

Figure 7 is an experimental electron micrograph of β(2) taken with the incident beam aligned parallel to the **a** axis of the triclinic cell ($\langle 211\rangle_F$). The image was acquired at about −900 Å defocus from a thin crystal fragment, however, the thickness could not be determined as the equal-thickness contours were not visible. The central triangular region clearly shows four strong white spots per cell. Furthermore, the

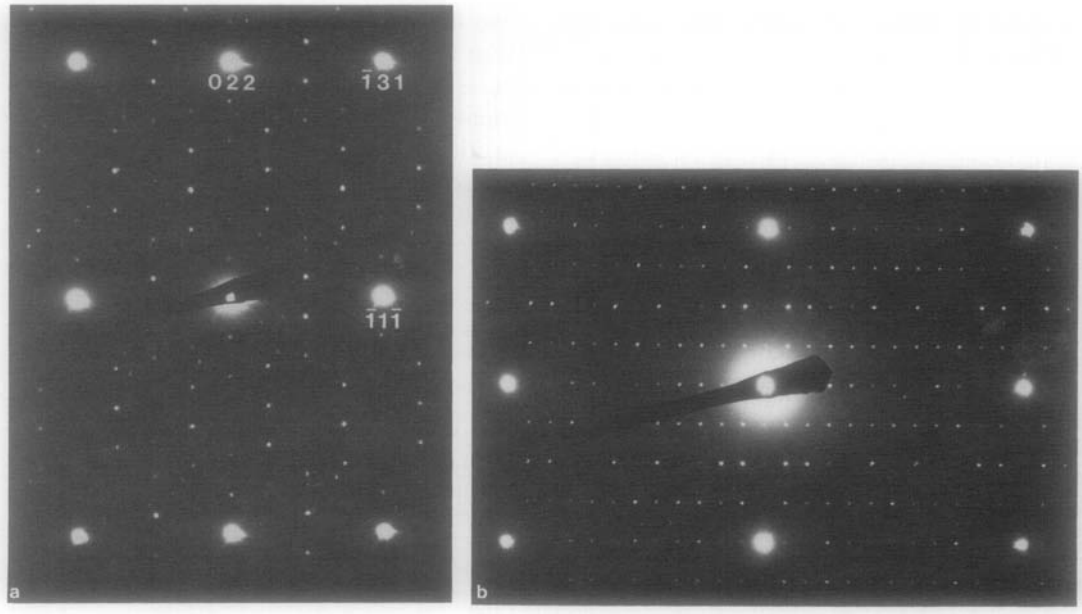

FIG. 6. Electron diffraction patterns ($\langle 21\bar{1}\rangle_F$ zone) of β-phase polymorphs observed in the TbO_x system.

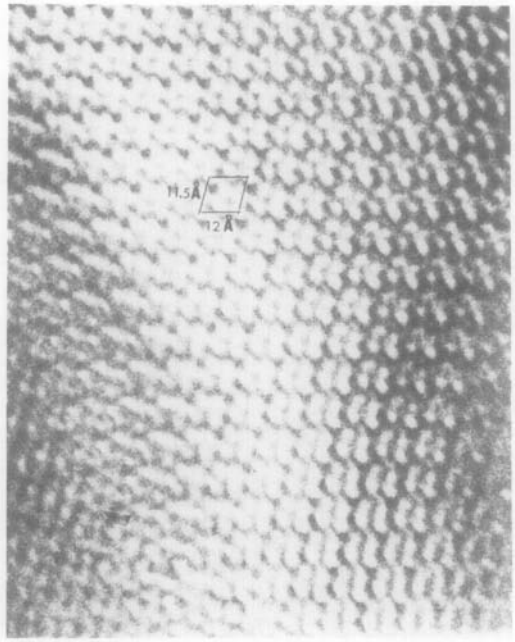

FIG. 7. Experimental bright-field image from a $\langle 100\rangle_{12}$ zone of $\beta(2)$ phase, $Tb_{24}O_{44}$.

white spots are arranged in pairs in an orientation similar to those in the crystal structure image of δ phase (Fig. 3). An intuitive interpretation of the image as vacancy pairs is suggested although the dynamical

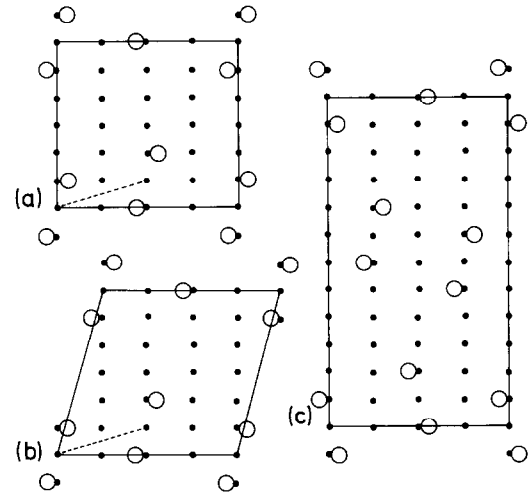

FIG. 8. $\langle 21\bar{1}\rangle_F$ projections of the proposed vacancy structures for the β-phase polymorphs in the PrO_x and TbO_x systems. (a) β, $Pr_{24}O_{44}$; (b) $\beta(2)$, $Tb_{24}O_{44}$; (c) $\beta(3)$, $Tb_{48}O_{88}$.

scattering effects including thickness and defocus conditions must be considered.

The structure proposed for the β phase in the praseodymium oxide system, which has monoclinic symmetry but has the same cell contents as $\beta(2)$ ($R_{24}O_{44}$) is shown diagrammatically in a $\langle 100 \rangle$ projection in Fig. 8a. Two octahedrally coordinated metal atoms lie at the origin and at $(\frac{1}{2}, \frac{1}{8}, \frac{1}{2})$, related by a $\frac{1}{2}[1\bar{2}1]_F$ vector. Oxygen vacancy pairs are oriented similarly about these two metal positions. Figure 8b shows the same projection for the $\beta(2)$ polymorph. The vacancies in the oxygen sublattice were placed analo-

TABLE II

ATOM POSITIONS[a] FOR THE PROPOSED STRUCTURE OF $\beta(2)$ PHASE, $Tb_{24}O_{44}$ SYMMETRY $P\bar{1}$

Atom	x	y	z	Atom	x	y	z
Tb1	0.000	0.000	0.000	Tb13	0.478	0.993	0.507
Tb2	0.604	0.826	0.048	Tb14	0.148	0.815	0.547
Tb3	0.273	0.649	0.0915	Tb15	0.750	0.667	0.583
Tb4	0.875	0.500	0.125	Tb16	0.375	0.500	0.625
Tb5	0.500	0.333	0.167	Tb17	0.012	0.337	0.682
Tb6	0.137	0.170	0.223	Tb18	0.625	0.167	0.708
Tb7	0.737	0.996	0.235	Tb19	0.250	0.000	0.750
Tb8	0.375	0.833	0.292	Tb20	0.863	0.829	0.777
Tb9	0.000	0.667	0.333	Tb21	0.500	0.667	0.833
Tb10	0.602	0.518	0.370	Tb22	0.125	0.500	0.875
Tb11	0.271	0.340	0.410	Tb23	0.727	0.351	0.912
Tb12	0.875	0.167	0.458	Tb24	0.396	0.174	0.952
O1	0.0625	0.8333	0.2542	O23	0.175	0.1667	0.3958
O2	0.8125	0.8333	0.6042	O24	0.9375	0.1667	0.6458
O3	0.0625	0.5000	0.6875	O25	0.5625	0.8333	0.8542
O4	0.8125	0.5000	0.9375	O26	0.3125	0.8333	0.1042
O5	0.5625	0.5000	0.1875	O27	0.3135	0.5000	0.4375
O6	0.5623	0.1667	0.5208	O28	0.3125	0.1667	0.7708
O7	0.1875	0.8333	0.7292	O29	0.8125	0.1667	0.2708
O8	0.6875	0.8333	0.2292	O30	0.3125	0.6667	0.2708
O9	0.6875	0.5000	0.5625	O31	0.3125	0.3333	0.6042
O10	0.6875	0.1667	0.8958	O32	0.3125	0.0000	0.9375
O11	0.4375	0.1667	0.1458	O33	0.8125	0.3333	0.1042
O12	0.4375	0.6667	0.6458	O34	0.0625	0.0000	0.1875
O13	0.4375	0.3333	0.9792	O35	0.1875	0.6667	0.8958
O14	0.9375	0.6667	0.1485	O36	0.6875	0.6667	0.3958
O15	0.1875	0.3333	0.2292	O37	0.6875	0.3333	0.7292
O16	0.1875	0.0000	0.5625	O38	0.4375	0.0000	0.3125
O17	0.9375	0.0000	0.8125	O39	0.0625	0.6667	0.5208
O18	0.6875	0.0000	0.0625	O40	0.8125	0.6667	0.7708
O19	0.4375	0.8333	0.4792	O41	0.0625	0.3333	0.8542
O20	0.4375	0.5000	0.8125	O42	0.5625	0.6667	0.0208
O21	0.1875	0.5000	0.0625	O43	0.5625	0.3333	0.3542
O22	0.9375	0.5000	0.3125	O44	0.5625	0.0000	0.6875
			Oxygen vacancies				
V1	0.0625	0.1667	0.0208	V3	0.9375	0.3333	0.4792
V2	0.9375	0.8333	0.9792	V4	0.8125	0.0000	0.4375

[a] Anion positions are all ideal fluorite positions. Cation positions are relaxed from ideal fluorite positions by a transformation from the refined ι-phase (Tb_7O_{12}) cation positions.

gously to those in $Pr_{24}O_{44}$ (i.e., across the body diagonal of MO_8 cubes centered at the origin and displaced by a $\frac{1}{2}\langle 1\bar{2}1\rangle$ vector). The vacancy coordinates are listed in Table II, together with ideal oxygen and relaxed metal positions.

Figure 9 displays a variety of calculated n-beam crystal structure images of $Tb_{24}O_{44}$ as a function of crystal thickness and defocus. These patterns were all computed for the atomic positions given in Table II and the actual experimental parameters of the microscope: $a = 0.285$ Å^{-1}, $c_s = 1.8$ Å, $\Delta = 120$ Å, $\theta_c = 0.9 \times 10^{-3}$ rad. The **a** axis length of 6.5 Å was used as the slice thickness. The interaction of 913 beams were included in the calculations. Again for this defective fluorite phase the oxygen vacancy image is calculated for the thinner crystals (<50 Å) at −900 Å defocus. In this case, however, the structural image repeats with thickness at 130 and 260 Å at −1100 Å defocus with very little distortion. The agreement between the calculated "vacancy" image and the contrast in Fig. 7 is satisfactory although the crystal may be thicker than 50 Å.

The cell parameters and fluorite axial relationships for the monoclinic polymorph of the β phase in the TbO_x system have been derived by Kunzmann and Eyring (*9*). The parameters for their choice of unit cell are $a = 6.7$ Å, $b = 23.2$ Å, $c = 15.5$ Å, $\beta = 125.2°$ with the following relationship to the substructure:

$$a = a_F + \tfrac{1}{2}b_F - \tfrac{1}{2}c_F,$$

$$b = 3(-b_F - c_F),$$

$$c = 2(-b_F + c_F).$$

This polymorph, which has twice the unit cell volume of β ($Pr_{24}O_{44}$) and $\beta(2)$ ($Tb_{24}O_{44}$), will be referred to as $\beta(3)$ ($Tb_{48}O_{88}$).

Figure 10 shows a $[21\bar{1}]_F$ zone experimental image of $\beta(3)$ on which the unit cell is delineated and the diffraction pattern inset. Part of the crystal had a very thin wedge shape as evidenced by the rather extensive area of uniform contrast near the edge. Since the optimum defocus value (−900 Å) was used and other conditions of the microscope and specimen were satisfied for imaging the projected crystal potential, the vacancy arrangement in this superstructure should be determinable from the image con-

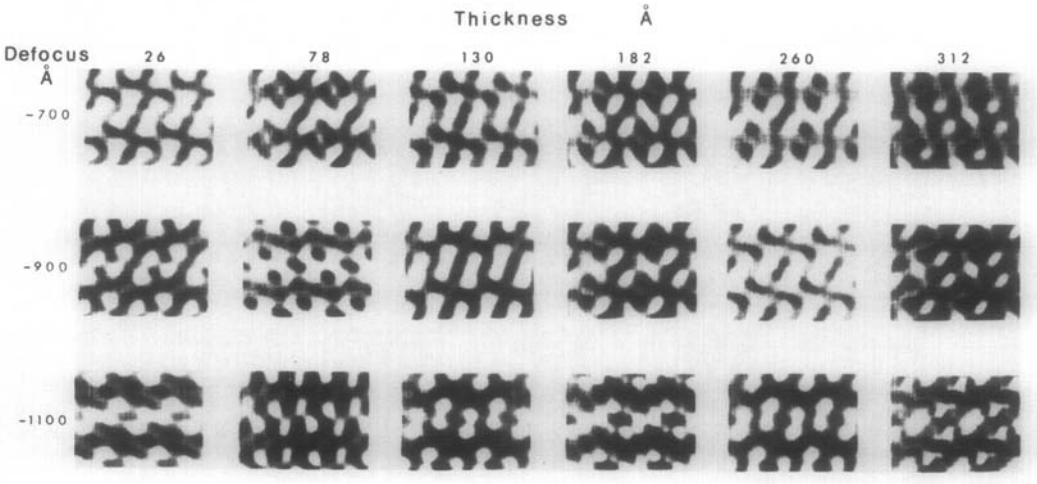

FIG. 9. Calculated $\langle 100\rangle_{12} = \langle 21\bar{1}\rangle_F$ crystal structure images of the proposed model of the $\beta(2)$ phase, $Tb_{24}O_{44}$.

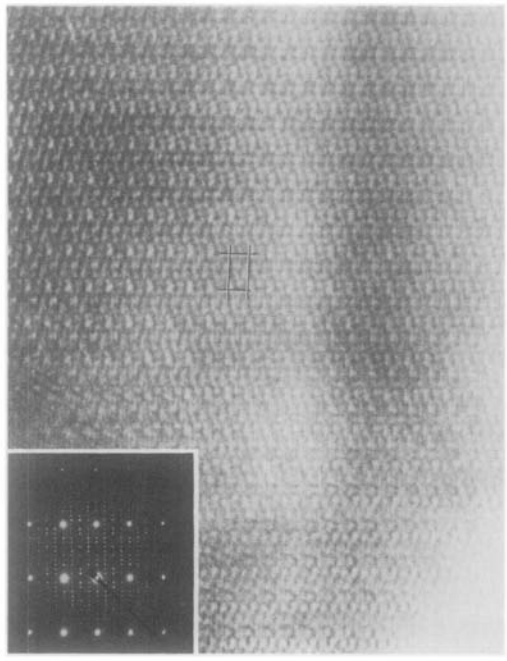

FIG. 10. The electron diffraction pattern and bright-field image from a $\langle 21\bar{1}\rangle_F$ zone of the $\beta(3)$ phase, $Tb_{48}O_{88}$.

trast. The idealized structure model derived from the bright field image is shown in Fig. 8c. All eight vacancies in this structure occur in pairs centered about the metal atoms at 0,0,0; $\frac{1}{2}$, $\frac{1}{6}$, $\frac{1}{2}$; $\frac{1}{4}$, $\frac{7}{12}$, $\frac{1}{4}$; $\frac{3}{4}$, $\frac{1}{2}$, $\frac{3}{4}$. The vector relating the first and last two vacancy pairs is a $\frac{1}{2}\langle 1\bar{2}1\rangle$ vector. Also, the pairs centered about $\frac{1}{4}$, $\frac{7}{12}$, $\frac{1}{4}$ and $\frac{3}{4}$, $\frac{1}{2}$, $\frac{3}{4}$ are separated from the other two by 11 $(135)_F$ planes.

Simulated crystal structure images calculated by the n-beam dynamical method for the proposed structural model of $Tb_{48}O_{88}$, Fig. 8c, are shown in Fig. 11. The same experimental parameters were included as in the calculated $\beta(2)$ images except 1500 beams were used in this case. Table III lists the ideal oxygen and relaxed metal positions on which the image calculations were based.

The structural relationships between the two β-phase polymorphs in the TbO_x system and the β phase in the PrO_x system can

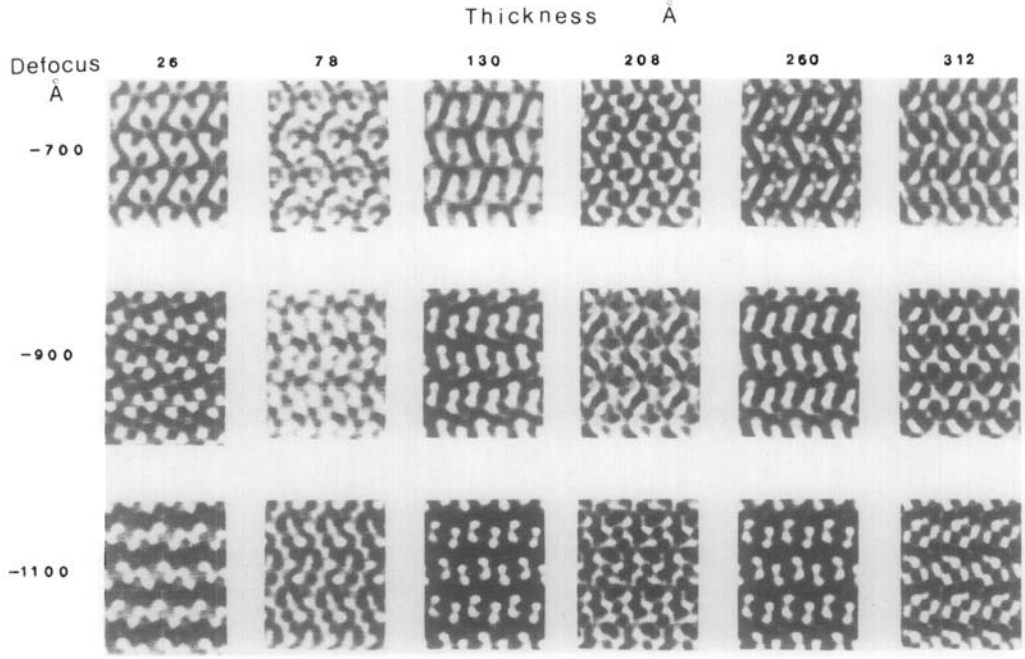

FIG. 11. Calculated $\langle 100\rangle_{12} = \langle 21\bar{1}\rangle_F$ crystal structure images of the proposed model of $\beta(3)$ phase, $Tb_{48}O_{88}$.

TABLE III

ATOM POSITIONS[a] FOR CALCULATED IMAGE OF $\beta(3)$-$Tb_{48}O_{88}$, MONOCLINIC, SYMMETRY P_n

Atom	x	y	z	Atom	x	y	z
Tb1	0.000	0.9167	0.750	Tb25	0.000	0.833	0.500
Tb2	0.500	0.4167	0.000	Tb26	0.9898	0.6755	0.7451
Tb3	0.0218	0.6736	0.5107	Tb27	0.9898	0.8245	0.9951
Tb4	0.000	0.500	0.750	Tb28	0.0311	0.6721	0.2451
Tb5	0.000	0.6667	0.000	Tb29	0.000	0.500	0.500
Tb6	0.9688	0.4946	0.2549	Tb30	0.0101	0.3279	0.7549
Tb7	0.000	0.3333	0.500	Tb31	0.9782	0.4931	0.9893
Tb8	0.000	0.1667	0.750	Tb32	0.000	0.333	0.250
Tb9	0.000	0.3333	0.000	Tb33	0.9688	0.1721	0.5059
Tb10	0.9782	0.1736	0.2393	Tb34	0.0218	0.9931	0.7607
Tb11	0.0311	0.9946	0.4951	Tb35	0.0101	0.1755	0.0049
Tb12	0.000	0.000	0.000	Tb36	0.000	0.000	0.250
Tb13	0.500	0.9167	0.750	Tb37	0.4898	0.9079	0.4951
Tb14	0.5218	0.9098	0.2607	Tb38	0.500	0.750	0.750
Tb15	0.500	0.750	0.500	Tb39	0.5311	0.9113	0.9951
Tb16	0.5311	0.5887	0.7451	Tb40	0.4898	0.5921	0.2451
Tb17	0.500	0.750	0.000	Tb41	0.500	0.5833	0.500
Tb18	0.500	0.5833	0.250	Tb42	0.4688	0.4113	0.7549
Tb19	0.4782	0.4098	0.4893	Tb43	0.5218	0.5902	0.0107
Tb20	0.500	0.250	0.750	Tb44	0.5101	0.4079	0.2549
Tb21	0.500	0.4167	0.000	Tb45	0.5101	0.2588	0.5059
Tb22	0.500	0.250	0.250	Tb46	0.4782	0.0902	0.7393
Tb23	0.500	0.0833	0.500	Tb47	0.500	0.250	0.000
Tb24	0.4688	0.0887	0.0049	Tb48	0.500	0.0833	0.250
O1	0.250	0.9167	0.5625	O45	0.250	0.9167	0.8125
O2	0.250	0.750	0.8125	O46	0.250	0.9167	0.3125
O3	0.250	0.250	0.5625	O47	0.250	0.750	0.5625
O4	0.250	0.750	0.3125	O48	0.250	0.750	0.0625
O5	0.250	0.5833	0.5625	O49	0.250	0.5833	0.3125
O6	0.250	0.4167	0.8125	O50	0.250	0.4167	0.5625
O7	0.250	0.5833	0.0625	O51	0.250	0.250	0.8125
O8	0.250	0.4167	0.3125	O52	0.250	0.4167	0.0625
O9	0.250	0.0833	0.8125	O53	0.250	0.250	0.3125
O10	0.250	0.250	0.0625	O54	0.250	0.0833	0.5625
O11	0.250	0.0833	0.3125	O55	0.250	0.0833	0.625
O12	0.750	0.9167	0.9375	O56	0.250	0.8333	0.9375
O13	0.750	0.9167	0.4375	O57	0.250	0.8333	0.4375
O14	0.750	0.750	0.6875	O58	0.250	0.6667	0.6875
O15	0.750	0.5833	0.9375	O59	0.250	0.500	0.9375
O16	0.750	0.750	0.1875	O60	0.250	0.6667	0.1875
O17	0.750	0.5833	0.4375	O61	0.250	0.500	0.4375
O18	0.750	0.250	0.9375	O62	0.250	0.3333	0.6875
O19	0.750	0.4167	0.1875	O63	0.250	0.1667	0.9375
O20	0.750	0.250	0.4375	O64	0.250	0.3333	0.1875
O21	0.750	0.0833	0.6875	O65	0.250	0.000	0.6875
O22	0.750	0.0833	0.1875	O66	0.250	0.000	0.1875
O23	0.750	0.8333	0.8125	O67	0.750	0.8333	0.5625
O24	0.750	0.8333	0.3125	O68	0.750	0.6667	0.8125
O25	0.750	0.6667	0.5625	O69	0.750	0.8333	0.0625
O26	0.750	0.500	0.8125	O70	0.750	0.500	0.5625

TABLE III—*Continued*

Atom	x	y	z	Atom	x	y	z
O27	0.750	0.6667	0.0625	O71	0.750	0.3333	0.8125
O28	0.750	0.500	0.3125	O72	0.750	0.500	0.0625
O29	0.750	0.3333	0.5625	O73	0.750	0.3333	0.3125
O30	0.750	0.1667	0.8125	O74	0.750	0.1667	0.5625
O31	0.750	0.3333	0.0625	O75	0.750	0.000	0.8125
O32	0.750	0.1667	0.3125	O76	0.750	0.1667	0.0625
O33	0.750	0.000	0.0625	O77	0.750	0.000	0.3125
O34	0.750	0.9167	0.6875	O78	0.250	0.8333	0.6875
O35	0.750	0.750	0.9375	O79	0.250	0.6667	0.9375
O36	0.750	0.9167	0.1875	O80	0.250	0.8333	0.1875
O37	0.750	0.750	0.4375	O81	0.250	0.6667	0.4375
O38	0.750	0.5833	0.6875	O82	0.250	0.500	0.6875
O39	0.750	0.4167	0.9375	O83	0.250	0.3333	0.9375
O40	0.750	0.5833	0.1875	O84	0.250	0.3333	0.4375
O41	0.750	0.4167	0.4375	O85	0.250	0.1667	0.6875
O42	0.750	0.250	0.6875	O86	0.250	0.000	0.9375
O43	0.750	0.250	0.1875	O87	0.250	0.1667	0.1875
O44	0.750	0.0833	0.4375	O88	0.250	0.000	0.4375
			Oxygen vacancies				
V1	0.750	0.0833	0.9375	V5	0.250	0.500	0.1875
V2	0.250	0.9167	0.0625	V6	0.750	0.6667	0.3125
V3	0.250	0.1667	0.4375	V7	0.750	0.4167	0.6875
V4	0.750	0.0000	0.5625	V8	0.250	0.5833	0.8125

[a] Oxygen positions are all ideal fluorite positions. Terbium positions are relaxed from ideal fluorite positions by a transformation from the refined ι-phase (Tb_7O_{12}) cation positions.

be seen from Fig. 8. $Tb_{24}O_{44}$ is a triclinic distortion from the monoclinic $Pr_{24}O_{44}$ structure with **a** and **b** axes in common but with the **c** axis comprising a $[233]_F$ vector instead of a $[110]_F$ vector. The oxygen vacancy locations in the two modifications are identical.

The monoclinic $Tb_{48}O_{88}$ structure has **a** and **c** axes in common with the monoclinic $Pr_{24}O_{44}$ cell, however, the **b**-axis length is doubled. All four six-coordinated metal atoms in the larger cell lie on alternate segments of $(135)_F$ and $(1\bar{5}\bar{3})_F$ planes analogous to those in the undoubled cell. The separation of planes of six-coordinated atoms alternates between 11 and 13 $(135)_F$ planes. The sum of these two planar spacings constitutes the **b**-axis length in $Tb_{48}O_{88}$.

Electron microscope images of crystals of terbium oxide often show an intergrowth of several intermediate phases. These intermixed crystals are sometimes observed in the initial stages of imaging, indicating that the product crystal of the hydrothermal growth method contains this type of disorder. In addition, many intergrowth structures are seen as reaction intermediates during reduction of high oxygen content phases by electron beam irradiation. One such intergrowth structure of the δ-$Tb_{11}O_{20}$ and $\beta(2)$-$Tb_{24}O_{44}$ phase is shown in Fig. 12. In this crystal two regions of $\beta(2)$ are separated by 30 unit cells of the δ phase. Notice that the projections of the body diagonal of the δ phase is the same as the projected cell edge of the $\beta(2)$ phase which makes these phases coherent.

$Tb_{16}O_{30}$

The first evidence for the existence of the

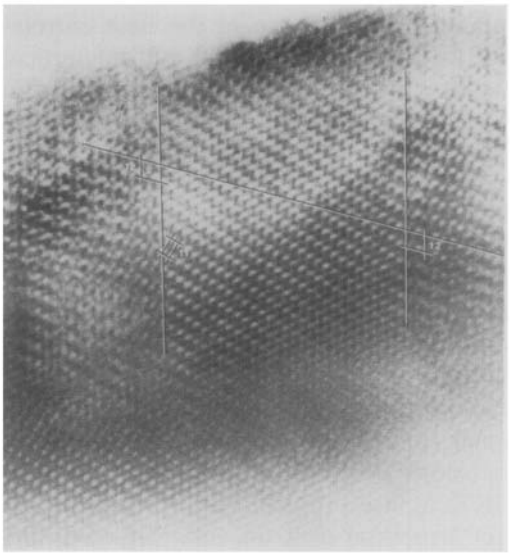

FIG. 12. Observed $\langle 21\bar{1}\rangle_F$ images of the intergrowth of the δ phase, $Tb_{11}O_{20}$, and the $\beta(2)$ phase, $Tb_{24}O_{44}$.

$n = 16$ member of the homologous series in the terbium oxide system has been obtained by electron diffraction and imaging. A superstructure consisting of eight $(02\bar{2})$ and two $(1\bar{1}1)$ fluorite planes is produced in the $\langle 21\bar{1}\rangle_F$ diffraction pattern shown in Fig. 13. If the $[2\bar{1}1]_F$ direction is an axial vector in the supercell, a common feature among all members of the R_nO_{2n-2} series, then a monoclinic unit cell with four times the volume of the fluorite cell can be defined as follows:

$$a = a_F + \tfrac{1}{2}b_F - \tfrac{1}{2}c_F,$$

$$b = 2(-b_F - c_F),$$

$$c = -b_F + c_F.$$

Using the lattice parameter for TbO_{2-x} ($0.1 < x < 0.2$) of 5.217 Å determined by Guinier powder diffraction data, the lattice

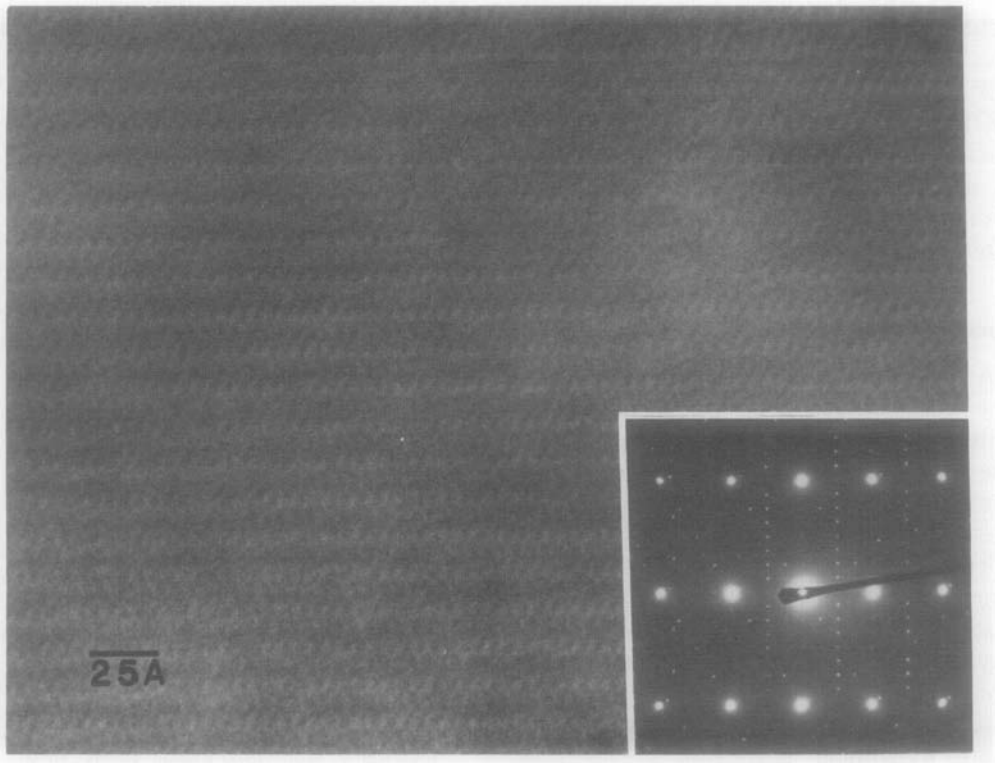

FIG. 13. Electron diffraction pattern and image of $Tb_{16}O_{30}$, $\langle 21\bar{1}\rangle_F$ zone.

parameters of the $n = 16$ superstructure are: $a = 6.4$ Å, $b = 14.8$ Å, $c = 7.4$ Å, $\beta = 125.2°$.

The image shown in Fig. 13 did not originate from a sufficiently thin area of the crystal to produce a projection of the crystal potential. The rectangular projection of the monoclinic cell, however, can still be seen in this view down the **a** axis. The structural principle which appears to relate all members of the R_nO_{2n-2} homologous series requires the two oxygen vacancies to be arranged in pairs separated by eight $(02\bar{2})_F$ planes in this structure.

The identification of the $Tb_{16}O_{30}$ phase is of interest since it is the most highly oxidized ordered intermediate phase belonging to the R_nO_{2n-2} homologous series of fluorite related phases in any binary rare earth oxide system. Mild heating of the crystallite of this phase was effected by concentrating with the second condenser lens current. Selected area diffraction showed a reduction to a mixture of $Tb_{24}O_{44}$ and $Tb_{11}O_{20}$. The fact that the $n = 16$ homolog (O/Tb = 1.875) was not detected in extensive tensimetric investigations in this system (*7, 8*) as well as its infrequency of occurrence with electron microscope observation indicates that this phase is only metastable.

Conclusions

A metastable phase, $Tb_{16}O_{30}$, has been discovered by electron optical techniques. This $n = 16$ member of the R_nO_{2n-2} sequence is the highest ordered intermediate phase known in the binary rare earth oxides.

The oxygen vacancy locations in three intermediate phases in the terbium oxide system ($Tb_{11}O_{20}$, $Tb_{24}O_{44}$, and $Tb_{48}O_{88}$) have been obtained by high-resolution electron microscope imaging. These are compared with images generated by multiple-beam dynamical scattering calculations. The proposed structures for these fluorite-related phases represent the best correlation between experimental and theoretical electron microscope contrast. Confirmation of these structures by X-ray or neutron diffraction intensity data is still necessary since a reliability factor has not been established for structural determinations by HRTEM.

HRTEM with a resolution of 1–2 Å will, however, be a powerful method for crystal structure investigation. Image intensity data are obtained from scattering through one dimension of a crystal (usually a very small thickness) rather than three dimensions for other structural methods. HRTEM also provides the only way to collect structural data on very defective and intergrown crystals.

It is likely that HRTEM will become more widely used for crystal structure determination in the future with advances in electron microscope instrumentation, specimen preparation methods and image-processing hardware and software.

Acknowledgments

Michael McKelvy's assistance with hydrothermal crystal growth is greatly appreciated. Also, it is a pleasure to thank the University Computer Center for use of their facilities. The National Science Foundation, through Grants DMR 77 08473 and DMR 80 06584, and under Grant CHE-7916098 (The Regional Instrumentation Center for High Resolution Electron Microscopy), has generously supported this work.

References

1. See "Direct Imaging of Atoms in Crystals and Molecules, Proceedings of the Forty-Seventh Nobel Symposium, Lidingö, Sweden, August 6–10, 1979" (Lars Kihlborg, Ed.); also, *Chem. Scripta* **14**, 295 (1978–79).
2. A. J. SKARNULIS, S. IIJIMA, AND J. M. COWLEY, *Acta Crystallogr. Sect. A* **32**, 799 (1976).
3. R. T. TUENGE AND L. EYRING, *J. Solid State Chem.* **29**, 165 (1979).
4. E. SUMMERVILLE, R. T. TUENGE, AND L. EYRING, *J. Solid State Chem.* **24**, 21 (1978).
5. L. EYRING *in* "Handbook on the Physics and

Chemistry of Rare Earths," Vol. 3 (K. Gschneidner and L. Eyring, Eds.), Chap. 27, pp. 337–399. North-Holland, Amsterdam (1979).
6. S. P. RAY, A. S. NOWICK, AND D. E. COX, *J. Solid State Chem.* **15,** 344 (1975).
7. B. G. HYDE AND L. EYRING, *in* "Rare Earth Research III" (L. Eyring, Ed.), p. 623. Gordon & Breach, New York (1965).
8. D. A. BURNHAM, L. EYRING, AND J. KORDIS, *J. Phys. Chem.* **72,** 4424 (1968).
9. P. KUNZMANN AND L. EYRING, *J. Solid State Chem.* **14,** 229 (1975).
10. P. E. CARO, *J. Less Common Metals* **16,** 367 (1968).
11. N. C. BAENZIGER, H. A. EICK, H. S. SCHULDT, AND L. EYRING, *J. Amer. Chem. Soc.* **83,** 2214 (1961).
12. R. B. VON DREELE, L. EYRING, A. L. BOWMAN, AND J. L. YARNELL, *Acta Crystallogr. Sect. B* **31,** 971 (1975).
13. S. P. RAY AND D. E. COX, *J. Solid State Chem.* **15,** 333 (1975).
14. M. Z. LOWENSTEIN, L. KIHLBORG, K. H. LAU, J. M. HASCHKE, AND L. EYRING, *Spec. Publ. Nat. Bur. Stand. USA* **364,** 343 (1972).
15. S. IIJIMA, *Acta Crystallogr. Sect. A* **29,** 18 (1973).
16. J. M. COWLEY AND S. IIJIMA, *Z. Naturforsch. A* **27,** 445 (1972).
17. J. M. COWLEY AND A. F. MOODIE, *Acta Crystallogr.* **10,** 609 (1957).
18. J. G. ALLPRESS AND J. V. SANDERS, *J. Appl. Crystallogr.* **6,** 165 (1973).
19. A. J. SKARNULIS, E. SUMMERVILLE, AND L. EYRING, *J. Solid State Chem.* **23,** 59 (1978).
20. M. A. O'KEEFE, *Acta Crystalogr. Sect. A* **29,** 389 (1973).